CERN – EUROPEAN ORGANIZATION FOR NUCLEAR RESEARCH

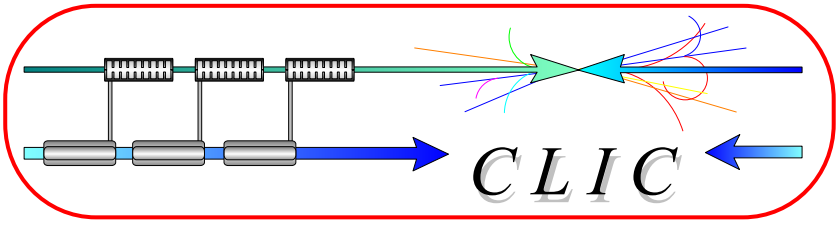

CLIC Note 656

30 GHZ RF COMPONENTS FOR CTF3

A. Grudiev, W. Wuensch, R. Fandos, S. Heikkinen, M. Taborelli and C. Achard.

Abstract

The rf and mechanical designs, and cold measurement results of CTF3 30 GHz rf components are presented. The power levels and pulse lengths to which a number of these devices have been operated is reviewed.

Geneva, Switzerland
April 2006

INTRODUCTION

The main activity of the CLIC high gradient structure development program is the high-power testing of accelerating structures in CTF3. The preparation of the experimental infrastructure for these tests has required the development of a wide range of high-power and diagnostic 30 GHz waveguide components. The small size, tight tolerances and high power required at 30 GHz have lead to a number of innovative designs of rf loads, directional couplers and diagnostic windows.

The design, cold measurement results and, in some cases, the performance at high power of these 30 GHz rf components are presented.

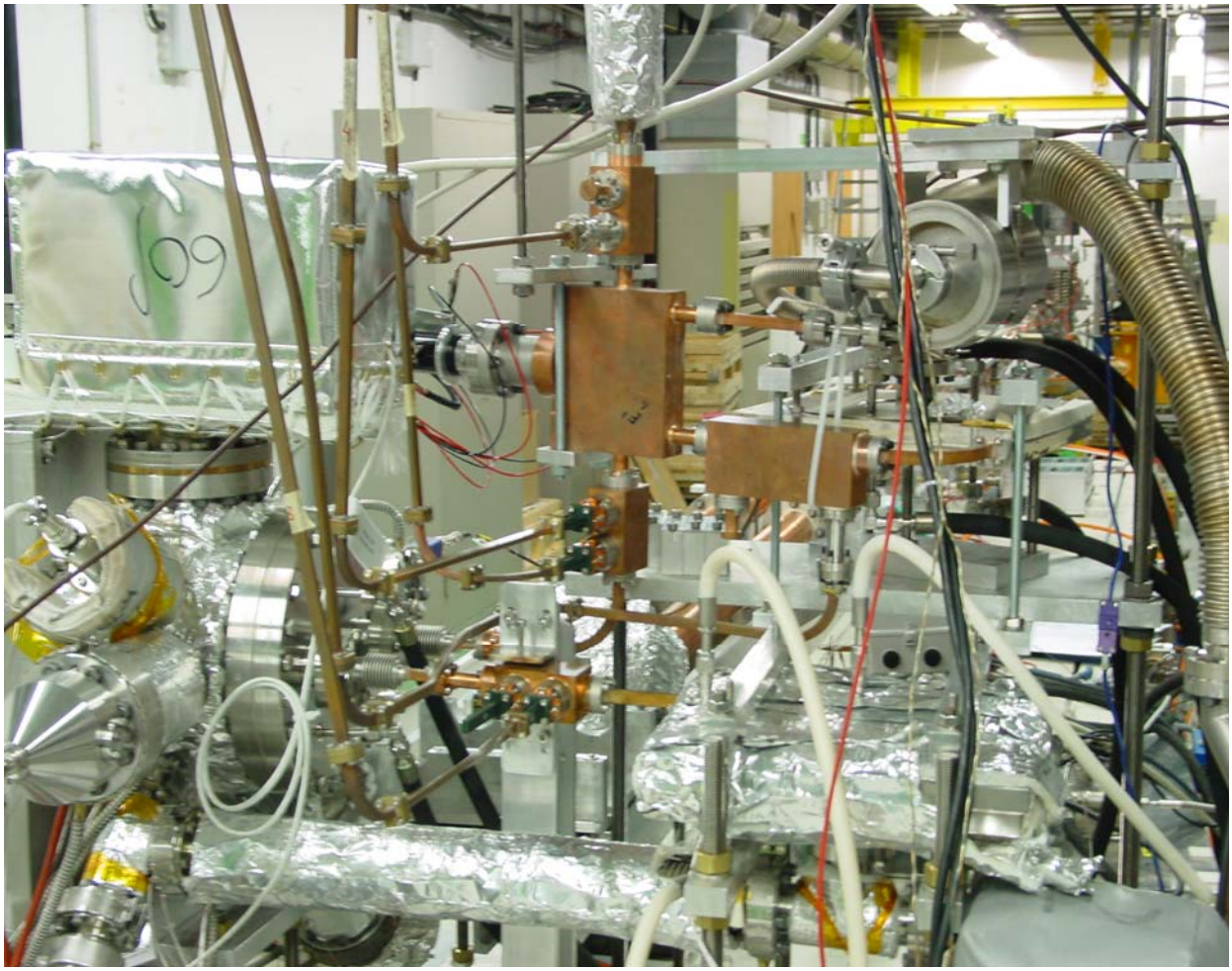

FIGURE 1. CTF3 30 GHz high power test stand.

HIGH POWER RF LOAD

At 30 GHz, a piece of stainless steel waveguide with high ohmic losses is an attractive solution for a high power rf load. The attenuation constant of the fundamental TE_{10} mode in a rectangular waveguide is

$$\alpha = \sqrt{\frac{\pi\rho}{\lambda Z_0}}\frac{1}{b}\left[\frac{1+\frac{2b}{a}\left(\frac{\lambda}{2a}\right)^2}{\sqrt{1-\left(\frac{\lambda}{2a}\right)^2}}\right] = 3.8\,dB/m\,,$$

where $a = 8.64mm$, $b = 3mm$ are the waveguide width and height, $\rho = 0.91\mu\Omega\cdot m$ is the resistivity of stainless steel, and λ and $Z_0 = 120\pi$ are the wavelength and the characteristic impedance in free space, respectively. For reflections below -40dB one requires about 5.5 m of such waveguide taking into account the return trip. Due to the small size and long length of the waveguide, vacuum pumping cannot be made just from the ends. It must be pumped along the waveguide. Early versions of 30 GHz loads in the form of a cylindrical spiral with many pumping holes suffered from excessively high rf reflections. Two new ideas have been proposed to introduce pumping without causing rf reflections. The first one is to bend the waveguide in the form of a spiral in the plane of the electric field as shown in Fig. 2. The second idea is to make a slot in the middle plane of the spiral. The slot connects all the waveguide turns in the radial direction to a vacuum pumping port in the center of the load. Since the pumping slot is cut in the plane which is not crossed by the rf currents associated with the fundamental TE_{10} mode propagating along the waveguide there is no rf coupling between the subsequent turns of the spiral load through the slot.

FIGURE 2. 2 halves of the high power rf load consisting of a 5.5 m long waveguide milled in a spiral form.

The radial cross-section of the spiral load is shown in Fig. 3 together with the pumping port, the 1mm-wide pumping slot, the spiral waveguide turns and the water cooling system. The assembly of the load does not require an rf contact between the two halves because no rf currents flow across the joint. Thus, no brazing is required, and welding or any other vacuum-compatible joining technique can be used. Both welded and brazed versions have been manufactured. An assembled load is shown in Fig. 4. The measured and analytical reflections from the load are presented in Fig. 5. The red measurement curve shows that the reflection is dominated by the reflections from the input flange but not by the reflections inside the load itself. The measured

reflection coefficient of about -35 dB is to be compared to the -42 dB analytical value. Nevertheless, this is a very good result and is more than sufficient for most applications. The load has been successfully tested in the CTF3 30 GHz high-power test stand shown in Fig. 1 up to the maximum available power (~55 MW@60 ns).

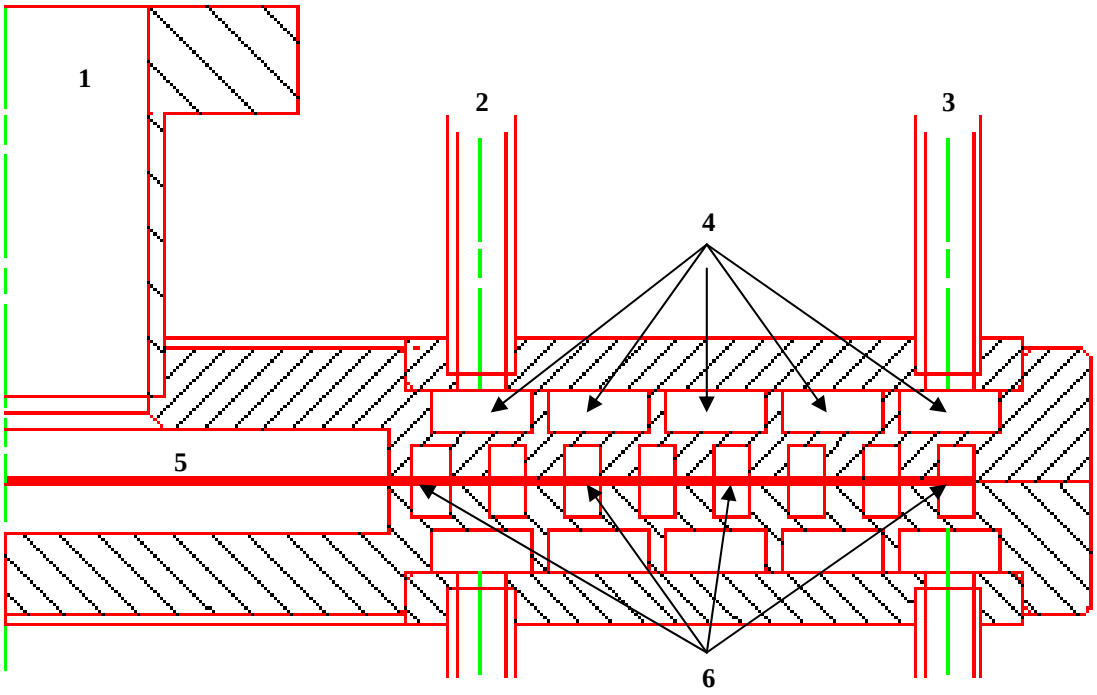

FIGURE 3. Cross-section of the spiral load: vacuum pumping port 1; water cooling system: inlet 2, outlet 3, and spiral channels 4; 1 mm wide pumping slot 5; and spiral waveguide cross-section 6.

FIGURE 4. The spiral load after assembly.

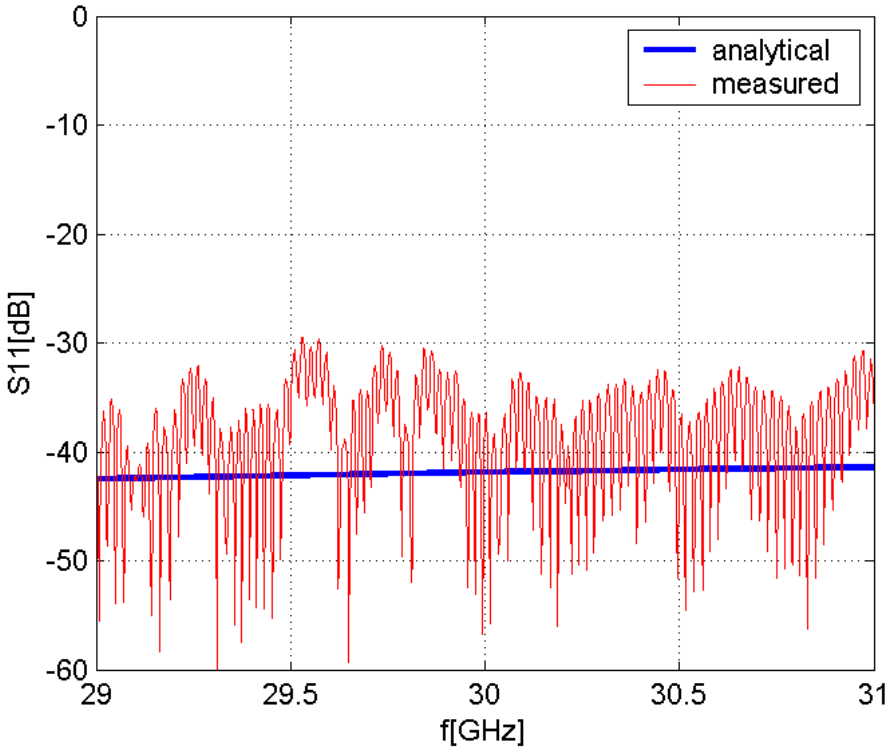

FIGURE 5. Measured (red) and analytical (blue) reflection coefficient of the spiral load.

H-PLANE DIRECTIONAL COUPLERS

This section describes the design and measurements of an H-plane directional coupler. The H-plane refers to rf coupling through holes in the smaller wall of the rectangular waveguide, and in which case the symmetry plane of the coupler is the plane parallel to the magnetic field lines of the fundamental TE_{10} mode. Since the electric field of the mode is zero near the holes the coupling is purely magnetic. The magnetic field distribution in the symmetry plane is shown in Figs. 6 (a) and (b) for two versions: a -30 dB coupler with 14 holes of 1.98 mm diameter and a -50 dB coupler with 8 holes of 1.38 mm diameter respectively. A difficulty with this design is that the thickness of the wall between adjacent waveguides is only 1mm. Moreover, good rf contact must be provided when joining the two halves of the coupler together. All these require delicate assembly and brazing. The machining and brazing have been done successfully for both designs and results are shown in Fig. 7. The measured and simulated S-parameters are presented in Fig. 8a and Fig.8b for the -30 dB and the -50 dB couplers respectively. The comparison of the measurements and simulations demonstrates rather good agreement for coupling and isolation but not so good agreement for reflections. The reflections are probably caused by the misalignment of the flanges and/or from the brazing joints inside the main waveguide. Nevertheless, the results are good and both couplers have been used in CTF3 and have seen powers and pulse lengths of 55 MW @ 60 ns. Table 1 summarizes the measured and simulated parameters of the couplers at 30 GHz.

a)

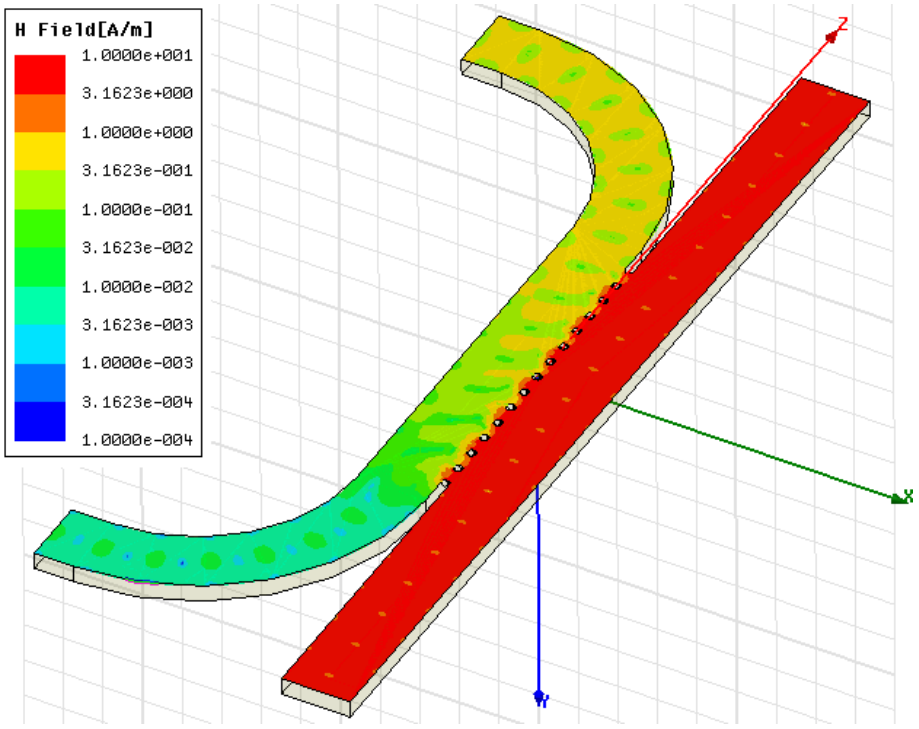

b)

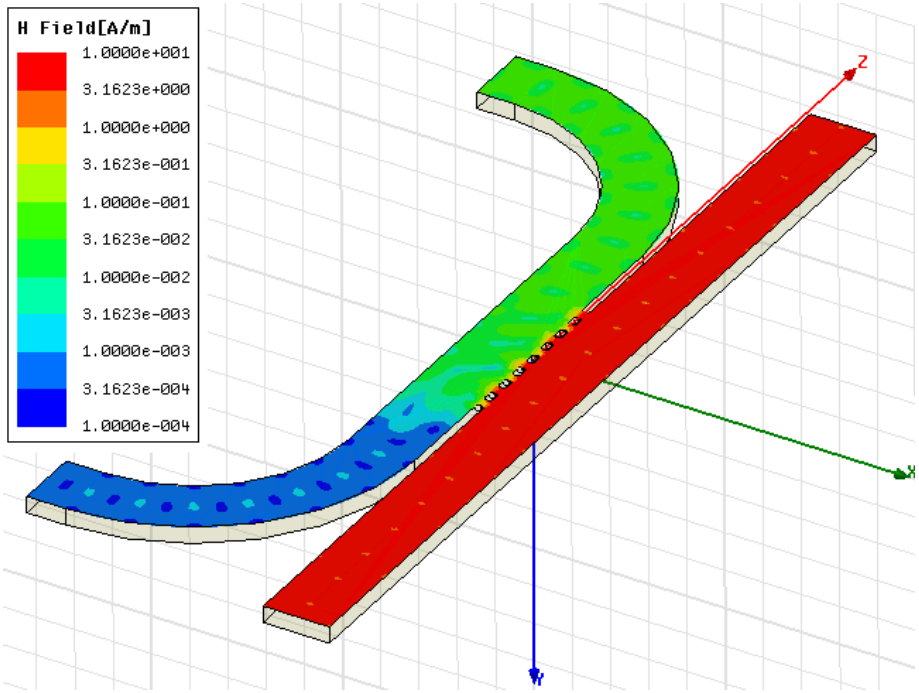

FIGURE 6. Magnetic field distribution in logarithmic scale is presented in the middle plane of symmetry in H-plane directional couplers: (a) -30 dB 14 holes coupler, (b) -50 dB 8 holes coupler.

FIGURE 7. View of H-plane directional couplers.

TABLE a). Parameters of two H-plane directional couplers at 30 GHz.

Parameter name	**14 holes (measured / simulated)**	**8 holes (measured / simulated)**
Coupling [dB]	-30 / -30	-50 / -50
Directivity [dB]	-35 / -35	-35 / -36
Reflection [dB]	-30 / -60	-25 / -56

a)

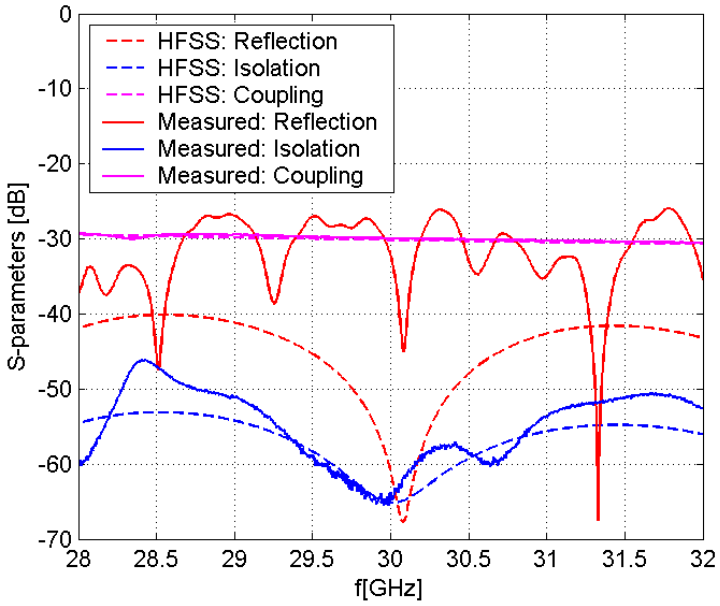

b)

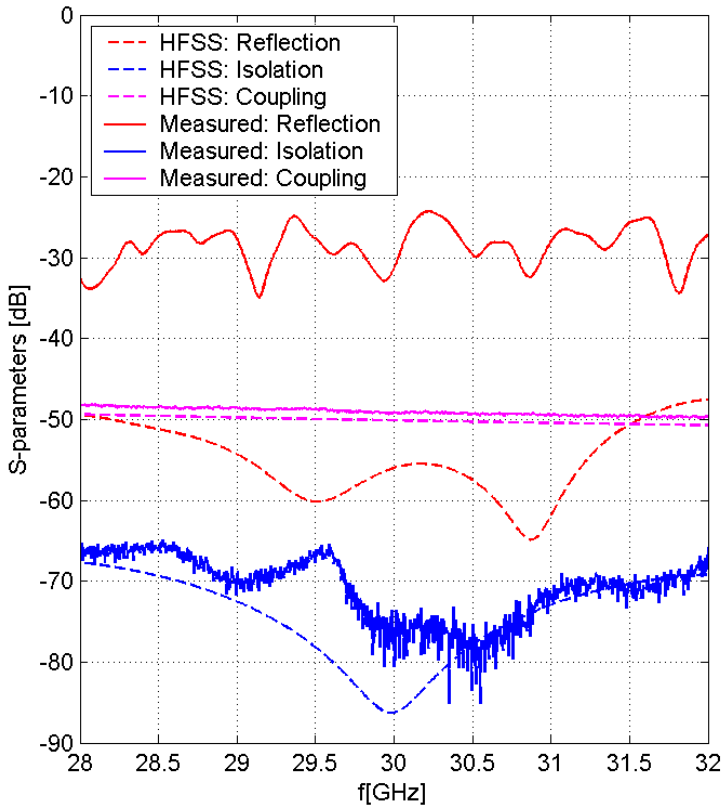

FIGURE 8. Measured and simulated S-parameters of H-plane directional couplers are presented by solid and dashed lines, respectively: (a) -30 dB 14 holes coupler, (b) -50 dB 8 holes coupler.

E-PLANE DIRECTIONAL COUPLERS

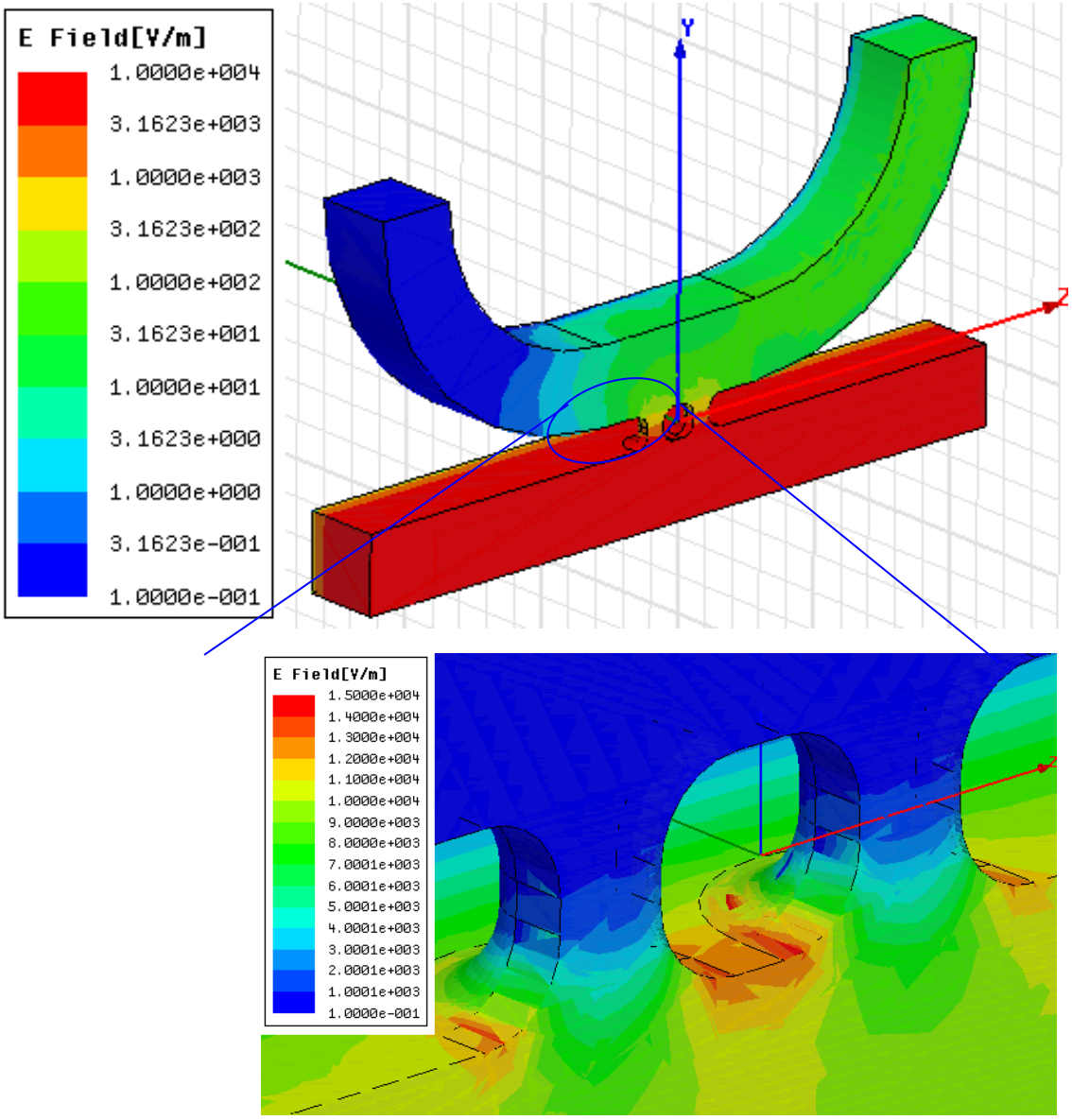

FIGURE 9. Electric field distribution (logarithmic scale) in an E-plane directional coupler. In the insert, electric field enhancement of about 20% in the region of the coupling holes.

Although the H-plane directional coupler presented in the previous section shows very good high and low power performances it has the shortcoming that it requires delicate assembly and brazing. An alternative E-plane directional coupler design which does not require brazing at all is presented in this section. Here the symmetry plane is parallel to the electric field lines of the fundamental TE_{10} mode. The electric field distribution in the symmetry plane and on the coupler walls is presented in Fig. 9. As one can see in Fig. 9 only two holes are necessary to provide practically any value of coupling because in the case of an E-plane coupler the coupling is stronger, since both the electric and magnetic fields are non zero in the region of the coupling holes. Assembly is simplified because rf currents associated with the fundamental mode do not

cross the symmetry plane. Thus, the coupler can be made from two symmetrical pieces without an rf contact between them so any vacuum compatible joining technique can be used. A disadvantage of the E-plane directional coupler is that, because the coupling holes are placed in the region of maximum surface electric field, there is an enhancement of surface electric field compared to that of a straight waveguide or an H-plane coupler. However, optimizing the shape of the holes to provide the required coupling on one side and to reduce the electric field on the other side results in only about a 20% electric field enhancement. The electric field distribution in the region of the holes is shown in Fig. 9 (insert). A smaller number of holes and a smaller waveguide bending radius (for the same mismatch) make the E-plane coupler more compact than the H-plane coupler described in the previous section.

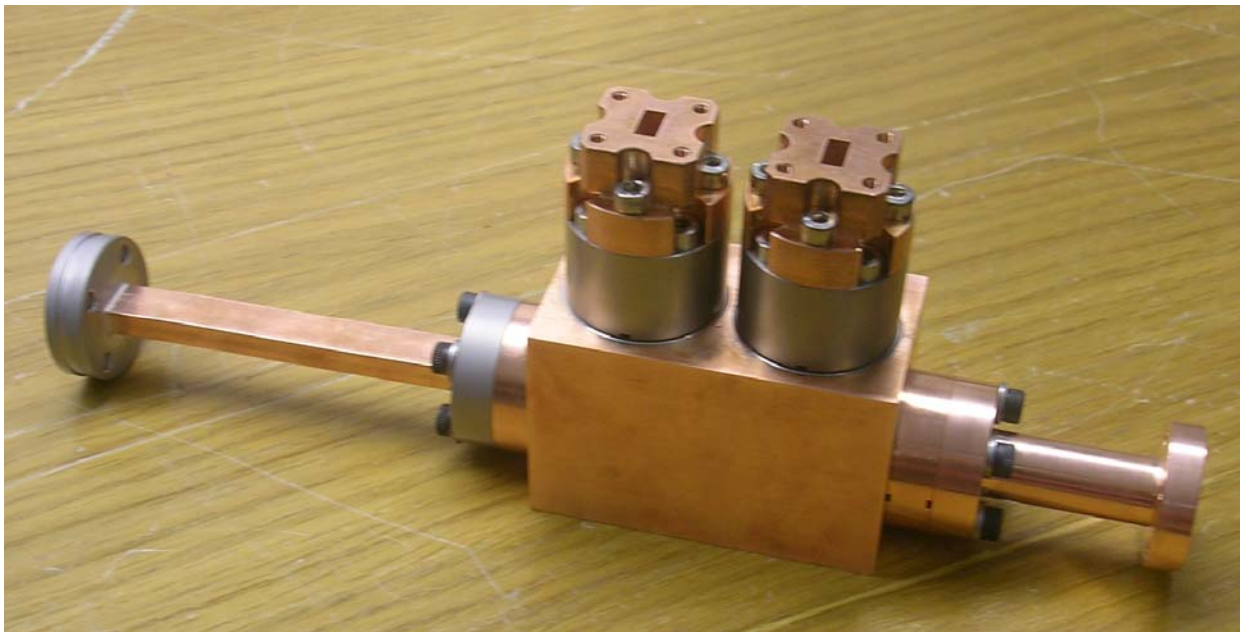

FIGURE 10. View of E-plane directional coupler with diagnostic rf windows.

An E-plane directional coupler assembled with two diagnostic rf windows discussed in the next section and input and output waveguide sections attached to it is shown in Fig. 10. It is about twice as small as the H-plane directional coupler. In Fig. 11, measured and simulated S-parameters of the H-plane directional coupler are presented demonstrating rather good agreement. At 30 GHz, the measured reflection coefficient is below -30 dB, the directivity is better then -35 dB and the coupling is -49 dB. Three directional couplers of the design presented in Fig. 10 have been tested in CTF3 30 GHz high power test stand up to the maximum available power (~55MW@60ns). They can be seen in Fig. 1 which shows the test stand layout.

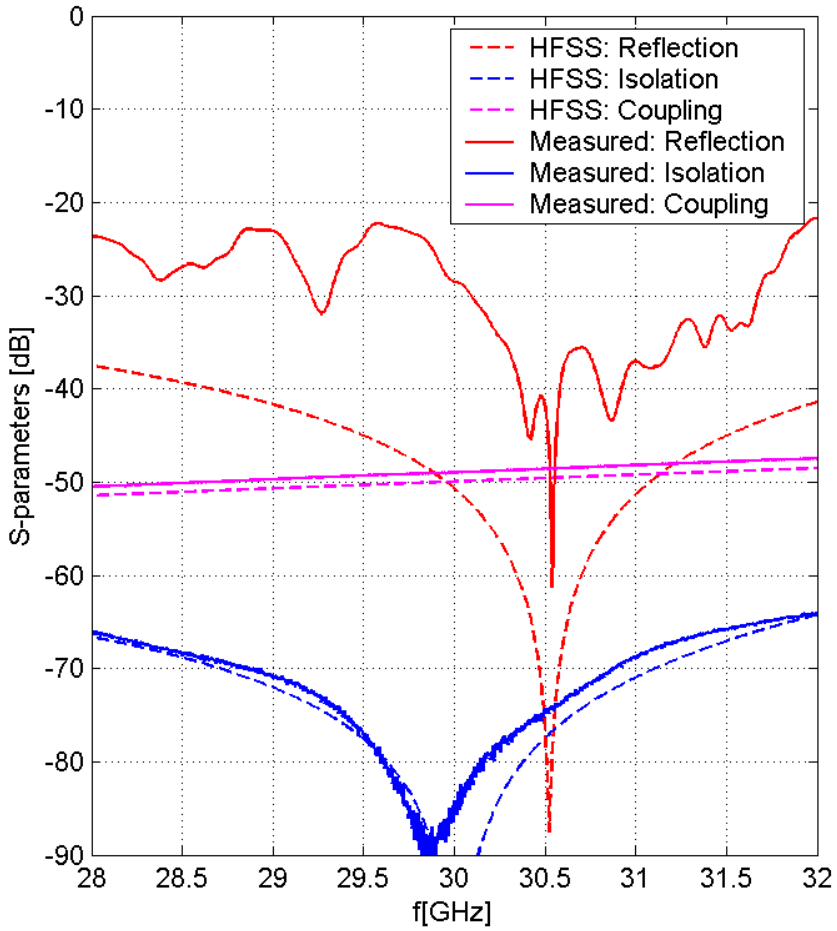

FIGURE 11. Measured and simulated S-parameters of E-plane directional coupler are presented by solid and dashed lines, respectively.

A special version of the E-plane directional coupler with a square cross-section main waveguide has also been designed based on the same principles. The electric field distribution in the symmetry plane and on the coupler walls is shown in Fig. 12. In this case, with the length of the side wall of the waveguide equal to 8.64 mm (the WR-34 width), 3 modes can propagate in the square waveguide. Two dummy holes are introduced opposite to the coupling-holes side of the square waveguide in order to keep the symmetry of the electro-magnetic fields and to avoid mode conversion. In Fig. 13, the computed value of the mode conversion is shown to be -70 dB for all high order modes both in reflection and in transmission. Fig. 13 also shows the S-parameters of the fundamental mode which are similar to the S-parameters for the rectangular waveguide E-plane coupler.

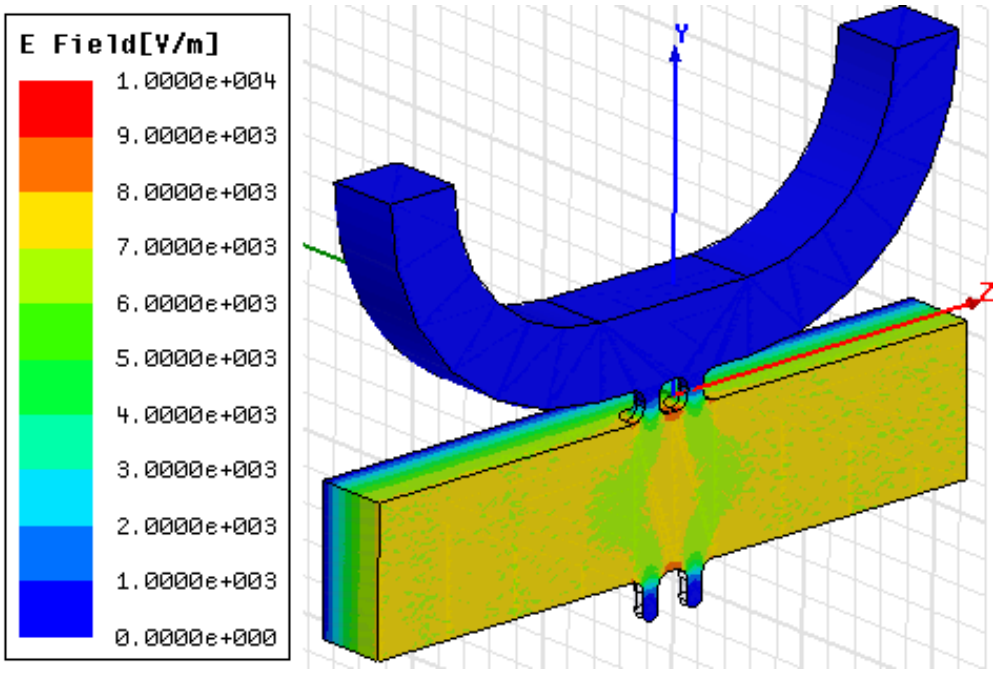

FIGURE 12. Electric field distribution in square waveguide directional coupler. Two dummy holes keep the symmetry of the electro-magnetic fields and reduce mode conversion.

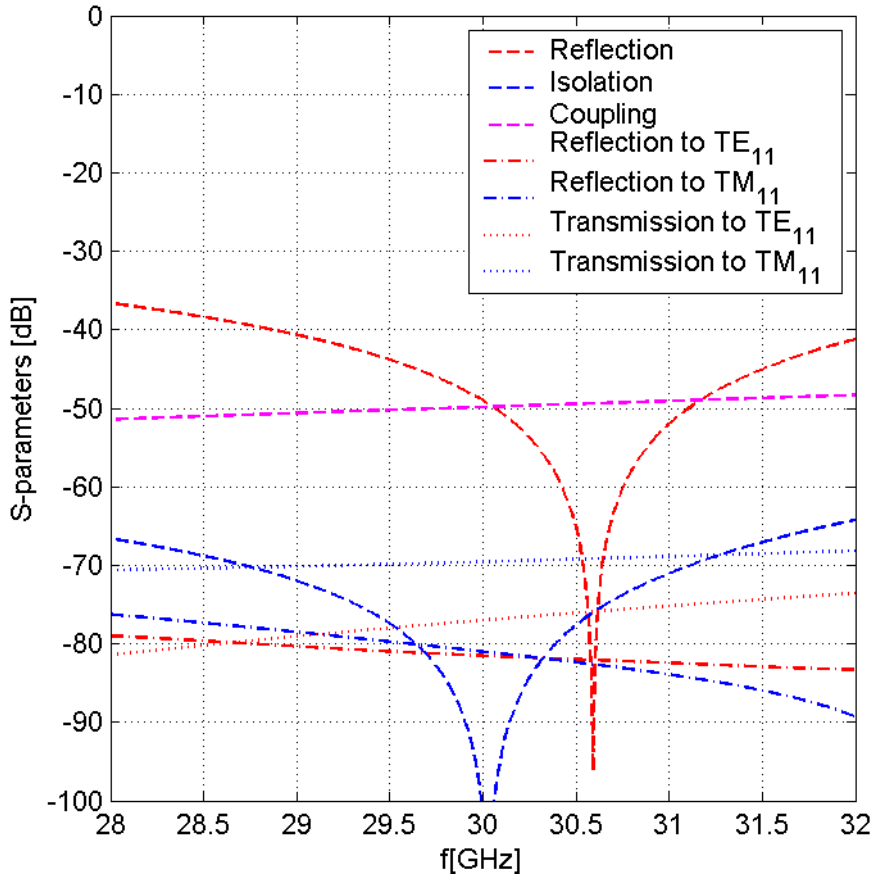

FIGURE 13. Simulated S-parameters of square waveguide directional coupler.

DIAGNOSTIC RF WINDOWS

In the CTF3 high power test stand, all high power waveguides are under vacuum however a transition to air must be made in the diagnostic waveguides which transfer the signals to the detecting electronics. At some point a low reflection rf window must be introduced to separate air and vacuum. A circular ceramic rf window has been designed for this low power diagnostic application. It consists of an up-taper from standard WR-34 rectangular waveguide to a short circular straight section and down-taper back to WR-34 waveguide. An alumina disk of about 10 mm diameter and 1.635 mm thickness is placed in the short circular straight section to separate air from vacuum but to maintain transmission of signals without reflections at the operating frequency. The instantaneous electric field distribution in circular ceramic rf window is shown in Fig. 14.

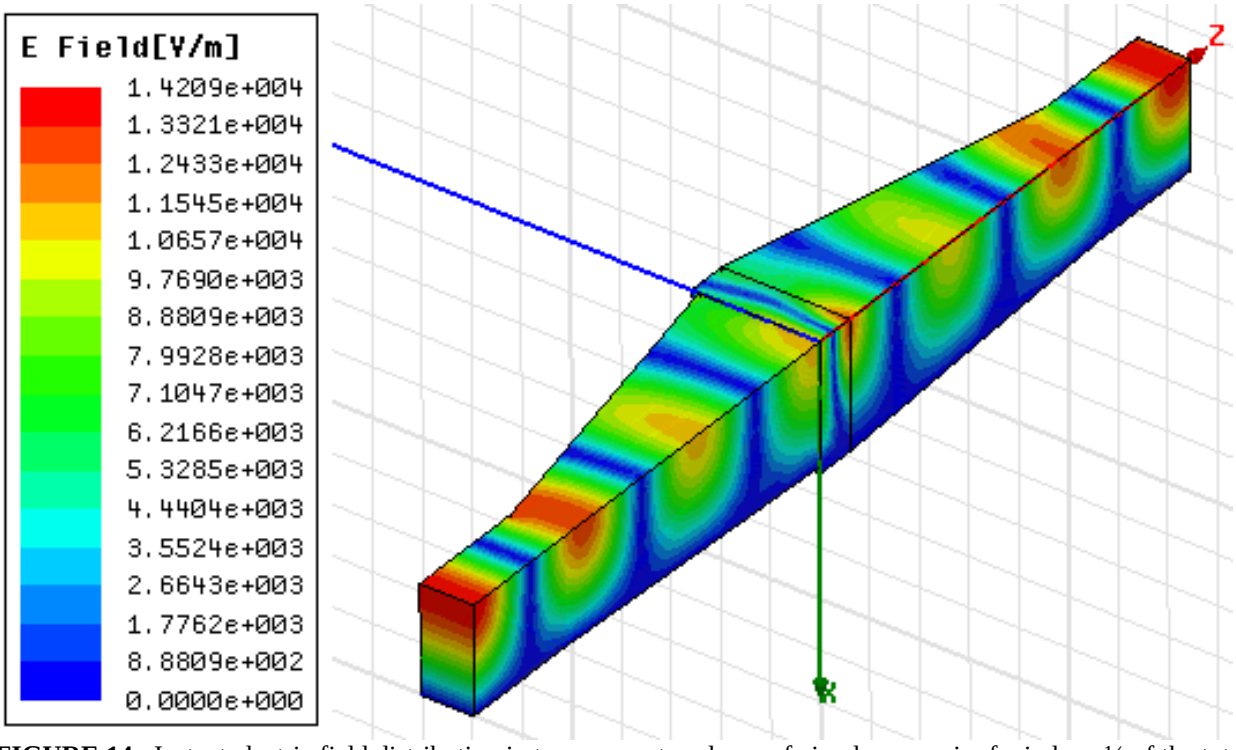

FIGURE 14. Instant electric field distribution in two symmetry planes of circular ceramic rf window. ¼ of the total geometry.

The ceramic disk has been fixed in the rf window by two methods: brazing and copper electroplating. In Fig. 15, a brazed rf window is shown before and after assembly. On the left, the white ceramic disk which is brazed in the titanium frame is visible. The measured and simulated reflection coefficient of the brazed rf window shown in Fig. 16 demonstrate a rather good agreement. Measured reflections are smaller than -30 dB allowing a single directional coupler to be used for measurement of both forward and backward signals.

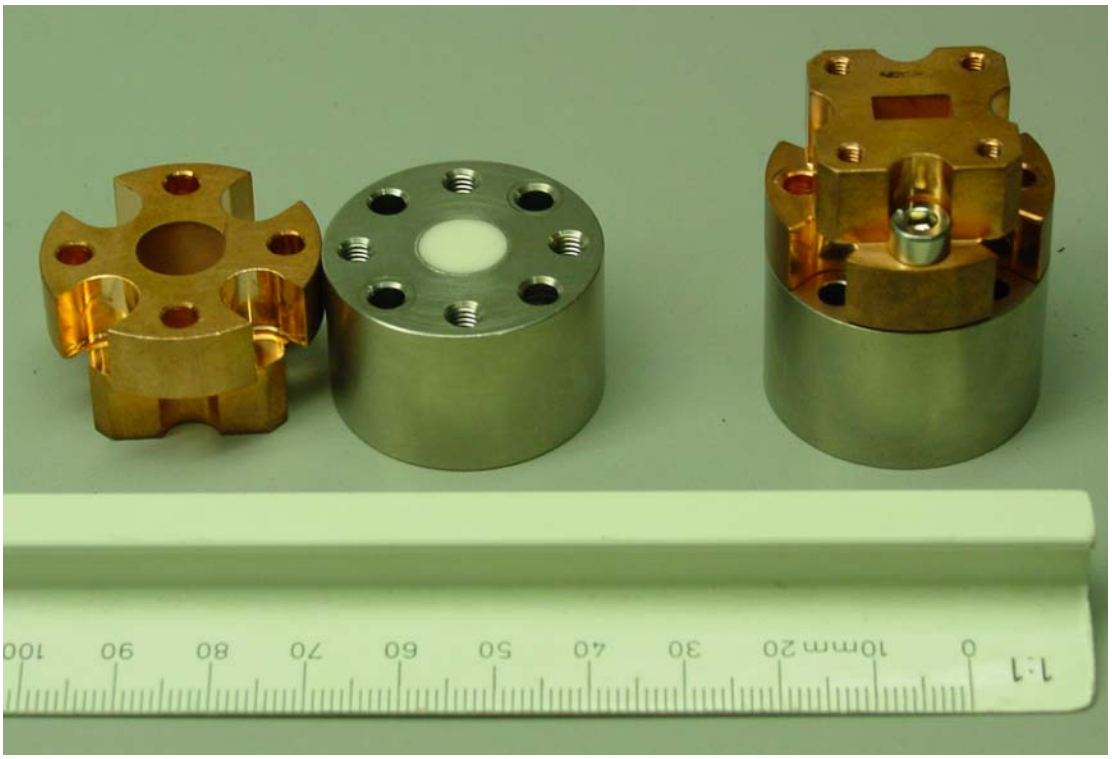

FIGURE 15. Brazed circular ceramic rf window is shown in disassembled (left) and in assembled (right) form.

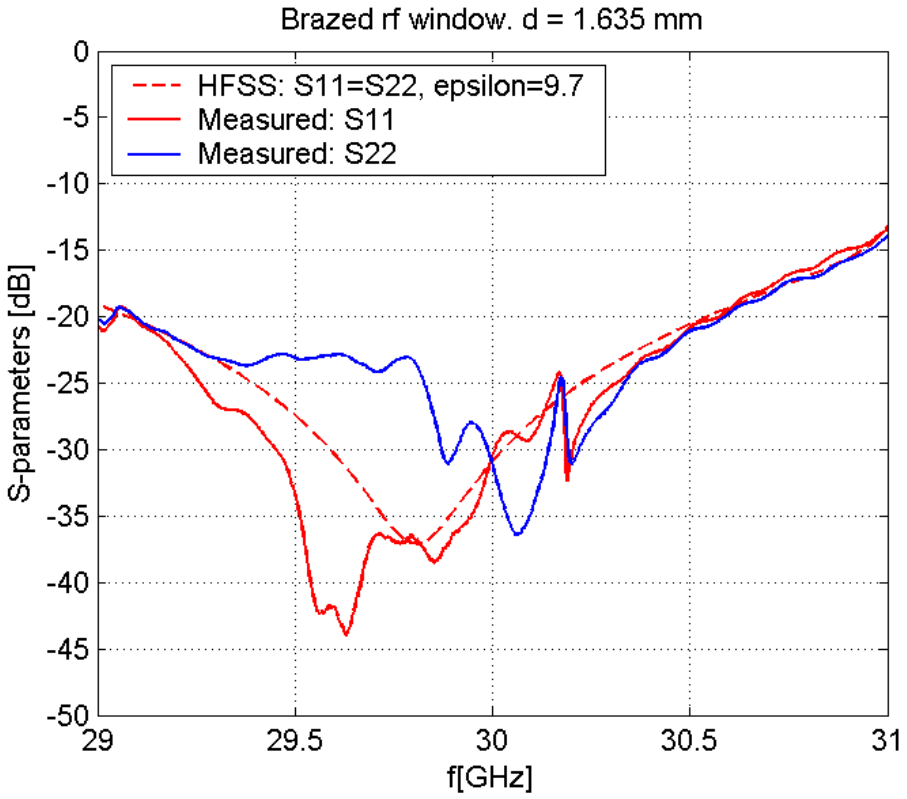

FIGURE 16. Simulated and measured reflection coefficient of brazed rf window.

a)

b)

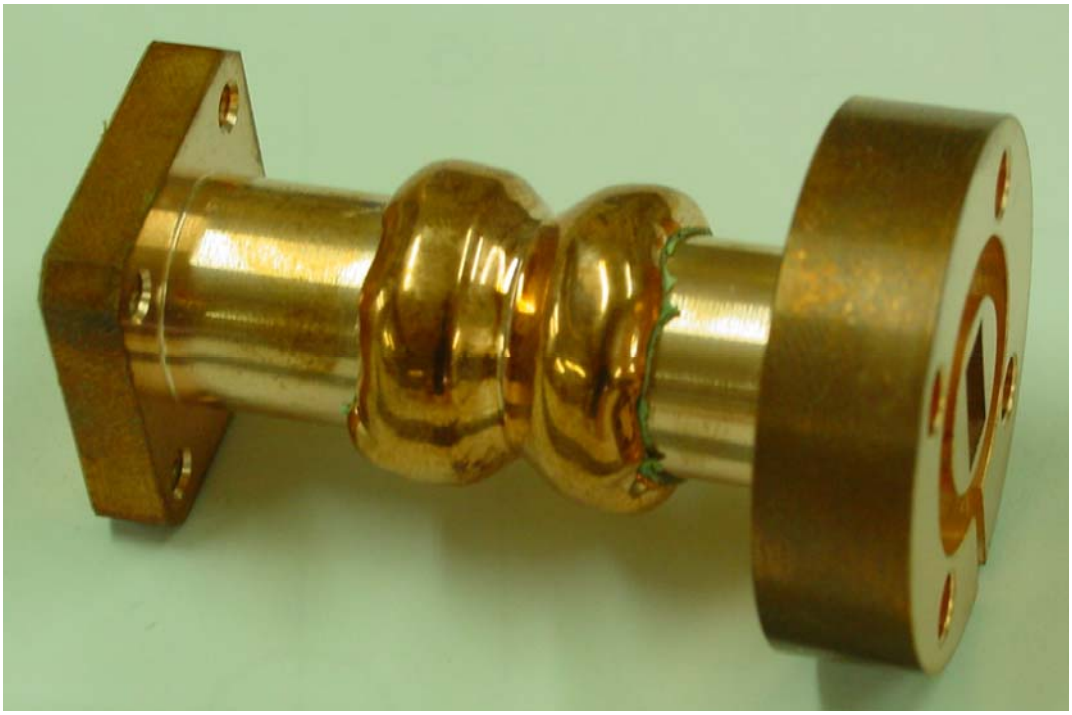

FIGURE 17. Cu-plated rf window before (a) and after (b) Cu-deposition.

In Fig. 17, a copper-plated rf window is shown before (a) and after (b) copper deposition. In Fig. 17 (a), the white ceramic disk with titanium followed by copper coating on the side is visible. This disk is clamped between two tapers which are also shown in Fig. 17 (a) and then the joint region is copper-plated to provide vacuum tightness. The measured and simulated reflection coefficient of the copper-coated window is presented in Fig. 18. Again the reflections are low (about -30 dB).

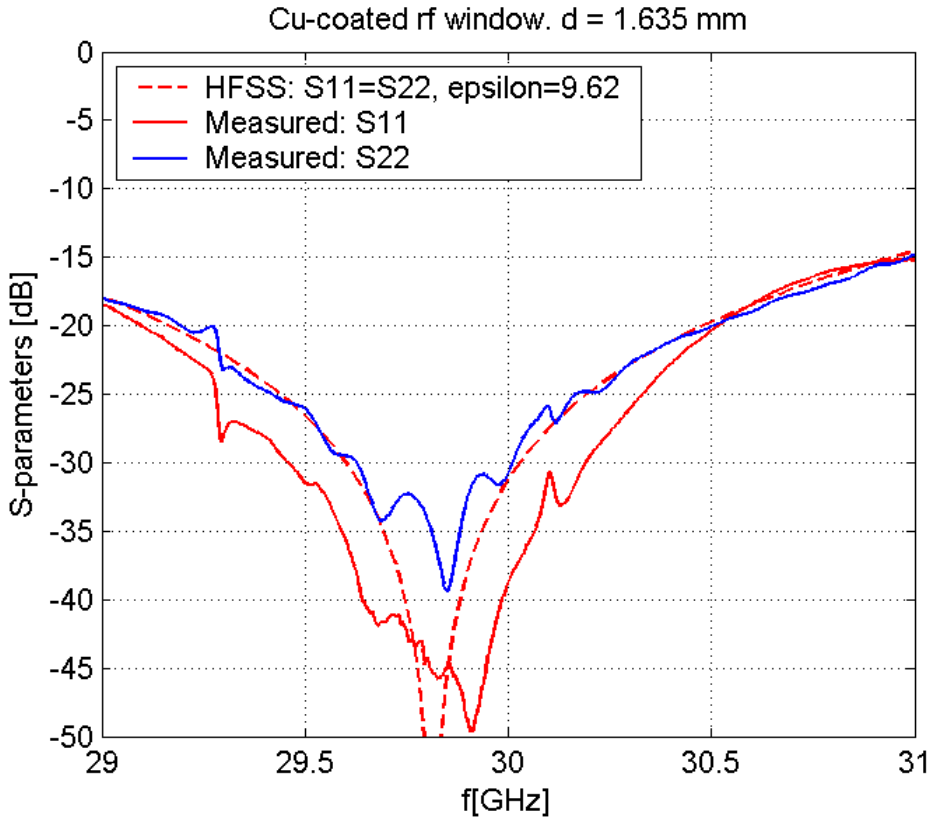

FIGURE 18. Simulated and measured reflection coefficient of Cu-plated rf window.